Electronic Supplementary Material (ESI) for ChemComm.
This journal is © The Royal Society of Chemistry 2023

Electronic Supplementary Information

Photo-enhanced electrochemical and colorimetric dual-modal aptasensing for aflatoxin B1 detection based on graphene-gold Schottky contact

Ya Wei, Yuye Li, Shuda Liu, Shuyun Meng, Dong Liu *, Tianyan You

Key Laboratory of Modern Agricultural Equipment and Technology (Jiangsu University), Ministry of Education, School of Agricultural Engineering, Jiangsu University, Zhenjiang, Jiangsu 212013, China

*Corresponding author: Dong Liu E-mail: dongliu@ujs.edu.cn

MATERIALS AND METHODS

Reagents

Streptavidin-coated magnetic beads (SMBs, 1 μm, Suzhou Beaver Biomedical Engineering Co., Ltd.), reduced graphene oxide (rGO, XFNANO Materials Tech Co., Ltd.), methylene blue (MB, ≥90%, Macklin), chloroauric acid ($HAuCl_4 \cdot 3H_2O$, 99.99%, Acros Organics), l-ascorbic acid (AA, 99.7%, Sinopharm Chemical Reagent Co., Ltd.), aflatoxin B1 (AFB1, 98.0%, Acros Organics), fumonisin B1 (FB1, 98.0%, Acros Organics), and ochratoxin A (OTA, 98.0%, Acros Organics) were used.

Tris hydroxymethyl aminomethane (Tris, 99.8%, Alfa Aesar), ethylene diamine tetraacetic acid (EDTA, ≥99.0 %, Adamas-beta), tris (2-carboxyethyl) phosphine (TCEP, ≥98.0%, Aladdin), Tween 20 ($C_{18}H_{34}O_6$, InnoChem Science & Technology Co., Ltd.) were used. Hydrochloric acid (HCl), sodium chloride (NaCl), magnesium chloride ($MgCl_2 \cdot 6H_2O$), potassium chloride (KCl), calcium chloride ($CaCl_2$), potassium dihydrogen phosphate (KH_2PO_4, ≥99.0%) and disodium hydrogen phosphate (Na_2HPO_4, ≥99.0%) were obtained from Sinopharm Chemical Reagent Co., Ltd.

DNA sequences were purchased from Sangon Biotech Co., Ltd. DNA sequences as follows (5'-3'):

•Aptamer (Apt): Biotin-GTT GGG CAC GTG TTG TCT CTC TGT GTC TCG TGC CCT TCG CTA GGC CCA CA (50 mer)

•Primer: SH-$(CH_2)_6$-CAA CTT CTA TGT GGG CCT AGC GAA (24 mer)

•Padlock: ACA TAG AAG TTG AAG CTG CTA CAA ACG GAG AAA GGA CTC GCA CAA CGC AAT CAG GTA TTC GCT AGG CCC (69 mer)

Buffers used in the experiment are as follows:

•Buffer Ⅰ (pH 7.4, 10 mM Tris-HCl, including 140 mM NaCl, 1 mM $MgCl_2$, 5 mM KCl, and 1 mM $CaCl_2$) was used to dissolve nucleic acid chains;

•Buffer Ⅱ (pH 7.4, 10 mM Tris-HCl, including 1 mM EDTA,1 M NaCl, and 0.1% Tween-20) was used to purify SMBs;

•Buffer Ⅲ (pH 7.4, 0.1 M PBS, including 0.1 M Na_2HPO_4, 0.1 M KH_2PO_4, and 0.1 M KCl)

acted as the working buffer.

Apparatus

Scanning electron microscope (SEM) images were collected on SU8020 SEM (Hitachi, Tokyo). Transmission electron microscopy (TEM) images were obtained with JEM 1200EX TEM (JEOL, Japan). X-ray electron spectra (XPS) were taken by a Thermo ESCALAB 250 instrument. The CS-420 colorimeter was obtained from Caipu Technology Co., Ltd. UVGO lamps with different wavelengths and intensities (365–450 nm, 0–7 W/cm^2, Zhongshan Yanming Technology Co., China) were used. EC measurements were conducted by Autolab PGSTAT 302N (Metrohm Co., Switzerland).

Zeta potential and dynamic light scattering (DLS) were measured by a Zetasizer Nano-ZS (Malvern Instruments, Malvern, U.K.). The ultraviolet-visible (UV-Vis) spectra were conducted by using a UV-2450 spectrophotometer (Shimadzu, Japan).

Electrochemical measurements

Electrochemical measurements used a conventional three-electrode system, comprising a modified glassy carbon electrode (GCE, 3 mm in diameter), a platinum wire counter electrode, and a saturated Ag/AgCl reference electrode (sat. KCl). The cyclic voltammetry (CV) measurement was performed with scan rate of 100 mV/s and alternating current voltammetry (ACV) was performed from 0 to -0.4 V with amplitude of 25 mV. The photocurrent and ACV responses were recorded in Buffer III containing 0.1 M AA. Electrochemical impedance spectroscopy (EIS) was tested by 5 mM $[Fe(CN)_6]^{3-/4-}$ in 0.1 M KCl solution and frequency range from 0.1 Hz to 10^5 Hz.

Preparation of rGO-AuNPs

rGO-AuNPs were synthesized according to a method reported previously with minor modifications.[1] First, rGO dispersion solution (2 mg mL^{-1}, 2 mL) was mixed with $HAuCl_4$ (1%, 2 mL) with magnetically stirring for 12 h. Then, the obtained solution was centrifuged (10000 rpm, 15 min) to collect the product and washed three times to

remove excess $HAuCl_4$. Finally, the resultant rGO-AuNPs nanocomposite was redispersed in 2 mL ultrapure water and stored at 4 °C for further use.

Preparation of Apt-Primer-MB SMBs

The equimolar ratio mixture of biotinylated Apt-AFB1 (10 μM, 120 μL) and Primer (10 μM, 120 μL) was heated at 95 °C for 10 min and then cooled to room temperature to obtain Apt-Primer. Then, MB (1 mM, 45 μL) was added into the mixture and further incubated at 37 °C for 1 h to obtain Apt-Primer-MB. SMBs (10 mg/mL, 100 μL) were washed with 1 mL buffer II for three times and resuspended in 450 μL buffer II for later use. Finally, 50 μL Apt-Primer-MB was added in SMBs suspension with gently shaking at 30°C for 75 min to obtain Apt-Primer-MB SMBs, followed by washing three times with buffer II.

CM detection of AFB1

100 μL AFB1 solution was mixed with the as-prepared Apt-Primer-MB SMBs with gentle shaking for 40 min at 37 °C. After magnetic separation, the supernatant was transferred to a new tube and recorded using a portable colorimeter to obtain RGB analysis. Data are presented as total color differences (ΔC) according to the Euclidean distance eq as follows:

$$\Delta C = \sqrt{(\Delta R)^2 + (\Delta G)^2 + (\Delta B)^2}$$

where ΔR, ΔG, and ΔB are the changes of R, G, and B values from blank values, respectively.[2]

PEEC detection of AFB1

The supernatant was hybridized with Padlock (100 μL, 2.5 μM) at 37 °C for 1 h to obtain Primer-Padlock-MB, and then TCEP (20 μL, 1 mM) was added for hydrosulphonyl activation at room temperature for 1 h. Glassy carbon electrode (GCE) was polished to a mirror luster stepwise by 0.05 μm alumina powder and ultrasonically cleaned with ethanol/water for 30 s sequentially. Then, 6 μL rGO-AuNPs and Primer-

Padlock-MB were dropped on GCE surface overnight at 4 °C. Later, the electrode was immersed in MB (200 μL, 5 μM) for 2 min, rinsed by buffer III and dried for alternating current voltammetry (ACV) detection.

Pretreatment of real samples

The fresh and moldy peanut and soil samples were obtained from Zhenjiang (Jiangsu Province). 5 g drying peanut or soil was dispersed in 20 mL extraction solution ($V_{methanol}$: V_{water} = 7:3). After shaking 60 min and then centrifuged at 8000 rpm for 15 min, the supernatant was filtered through a 0.22 μm ultrafiltration membrane by syringe filter. Finally, a series of AFB1 standards were added to the supernatant and stored at 4 °C for further use. The standard test method (HPLC-FL) was employed as validation. This testing was done at ICAS Testing Technology Service Co., Ltd (Shanghai) with an Agilent 1290 Infinity UHPLC coupled to FL spectrometer.

SUPPLEMENTARY RESULTS

Photoelectric performance of rGO

As shown in Fig. S1B, rGO shows more intensive absorption in the ultraviolet light region in the ultraviolet-visible (UV-vis) spectrum, exhibiting the absorption peak at 266 nm according to the π→π* transition assigned to the aromatic C=C bond.[3] The photocurrent response of rGO exhibits good consistency with the absorption spectrum and the highest photoresponsivity was observed at 365 nm (Fig. S1C). In addition to the wavelength dependency, the influence of the incident light intensity was further explored, as shown in Fig. S1D, the current response increases almost linearly with the intensity from 0.7–7.0 W/cm^2. Therefore, the 365 nm light source with 7.0 W/cm^2 was selected as the input signal to stimulate substrate material. Additionally, the photocurrent intensity of rGO-AuNPs remains at 96.7% of the original value even after 1000 seconds measurement cycles, indicating satisfactory stability (Fig. S1F).

Calculation of energy band position of rGO-AuNPs

Based on valence band XPS (VB-XPS) and UV−vis spectra, the band structure of rGO-AuNPs could be identified. Due to band-bending and enhancement of potential barriers in the formation of Schottky contact, the band gap of rGO-AuNPs decreases to 1.80 eV, which is conducive to the electron transfer for the semiconductor (Fig. S2A).[4] The rGO has been confirmed to possess the characteristics of n-type semiconductors, which band structure strongly depends on C/O ratio.[5] As shown in Fig. S2A and Fig. S2B, the band gap value, VB, and conduction band (CB) energy level of rGO are reckoned as 2.15 eV, +0.46 eV, and -1.69 eV, respectively. The rGO was analyzed using XPS to confirm C/O content ratio. As shown in Fig. S2C, the wide scan spectra of rGO shows photoelectron lines at binding energies of 284.5 eV and 529.8 eV which are ascribed to C1s and O1s, respectively, which contains 4.31 atom% O and 95.69 atom% C.[6]

The calculation process of band energy value is as follows: Tauc plots are estimated from the UV-vis spectra to determine band gap energies (E_g). Based on the relationship between $(\alpha h\nu)^{1/n}$ and photoelectron energy ($h\nu$), the band gap energy of the composite structure can be calculated by the following formula:

$$(\alpha h\nu)^{1/n} = A\,(h\nu - E_g)$$

where α and h are the absorption coefficient and Planck constant, respectively. ν, A, and E_g are the light frequency, proportional constant, and band gap energy, respectively.[7] The value of n is directly related to the transition type of semiconductor. rGO is the direct band gap type semiconductor, and the value of n is 1/2.[8] The band gaps of Tauc plots are evaluated by determining the X-intercepts of the tangents.

The conduction band (CB) energy level of rGO was evaluated by the following formulas:

$$E_{CB} = E_{VB} - E_g$$

The valence band (VB) energy level of rGO was evaluated by the valence band XPS (VB-XPS) spectra. The linear part of the VB-XPS spectra near 0 eV is extrapolated to intersect with the horizontal extension line, and the intersection point is E_{VB}.[9]

Characterization of Apt-Primer-MB SMBs

The synthesized Apt-Primer-MB was connected with SMBs via biotin-streptavidin interaction. After the modification of SMBs with magnetic separation, the absorbance intensity at 663 nm of Apt-Primer-MB in the supernatant decreases, indicating that the content of Apt-Primer-MB decreases (Fig. S3A). Zeta potential of Apt-Primer-MB and SMBs are -5.3 mV and -26.6 mV, respectively. After incubating Apt-Primer-MB with SMBs, Zeta potential decreases to -41.1 mV (Fig. S3B). SMBs demonstrate a diameter of 1000 nm by DLS measurements and the diameter increases after connecting with Apt-Primer-MB (Fig. S3C). These results indicate that Apt-Primer-MB is successfully assembled on the SMBs.

Characterization of construction of electrode interface

CV measurements toward $[Fe(CN)_6]^{3-/4-}$ redox and AA oxidation were performed to characterize the fabrication process of electrode interface. As shown in Fig. S4A, symmetric redox peaks appear on the bare GCE corresponding to the reversible redox reaction of $[Fe(CN)_6]^{3-/4-}$ (curve a). After the modification of rGO-AuNPs, the peak current increases due to the excellent conductivity of rGO (curve b). As the following modification of Primer-Padlock-MB and incubation with MB, the peak current increases successively for the interaction between the MB and $[Fe(CN)_6]^{3-/4-}$ (curve c and d). As shown in Fig. S4B, compared with bare GCE (curve a), oxidation peak of AA increases after modifying rGO-AuNPs. Upon the assemble of Primer-Padlock-MB, the peak current decreases due to the steric blocking effect (curve c). After incubation with MB, the peak current remarkably increases owing to the redox reaction between the MB and AA (curve d).

The electrolyte interfacial resistance and charge transfer resistance of electrode interface were proved by the Bode plots obtained from EIS measurements (Fig. S4C). The low-frequency region reveals charge transfer ability of electrode, while at the high frequency region, the total impedance is governed by the ohmic resistance of the electrolytic solution, and thus the phase is close to 0°.[10, 11] Due to superior electron-

transfer capability, the rGO-AuNPs-modified electrode exhibits a lower impedimetric value than bare GCE (curve a and b). With the sequential assembly of Primer-Padlock-MB and MB, the impedimetric value decreases successively (curve c and d). The result is consistent with above CV measurements. A Bode phase angle plot against frequency is shown in Fig. S4D. Compared with bare GCE, the maximum frequency peak appears remarkable decrease with further modification of rGO-AuNPs, Primer-Padlock-MB and immersion of MB, which indicates the lowest reaction resistivity between the electrolyte and electrode. These results indicate the successful fabrication of electrochemical sensing interface for AFB1.

Optimization of conditions

The load density of double strand on SMBs affect the recognition sensitivity of target-Apt, thus it is necessary to optimize the incubation time between SMBs and Apt-Primer-MB. As shown in Fig. S6A, with the extension of incubation time, ΔC gradually increases and reaches the maximum at 75 min. With time prolonging continually, the double-strand distribution density on the SMBs increases, weakening specific recognition ability and decreasing the released content of MB. Therefore, 75 min was selected as the optimal incubation time between SMBs and Apt-Primer-MB for subsequent experiments. As shown in Fig. S6B, as the incubation time between AFB1 and Apt-Primer-MB SMBs increasing, I_{MB} increased and then keep a stable platform at 30 min, indicating that the specific recognition between AFB1 and Apt reached saturation. To ensure the stability of the aptasensor, 40 min was selected as the optimal target incubation time.

Selectivity, reproducibility, and stability

AFB1 with the concentrations of 1 ng mL^{-1} and 20 ng mL^{-1} were employed for CM and PEEC sensing mode performance investigation, respectively. Given the complexity of the contaminated samples in real time analysis applications, OTA, ZEN, and FB1 as potential interfering mycotoxins were added to assess the selectivity of the developed

aptasensor. As illustrated in Fig. S7A and Fig. S7D, compared with the signal intensity generated by AFB1, the signal response is negligible for interfering substances with 10-fold concentration, indicating the aptasensor possessed satisfactory selectivity.

Stability and reproducibility are critical factors to assess the practicality of aptasensors. The reproducibility was evaluated by 7 parallel measurements. ΔC and I_{MB} with light off and on were obtained with relative standard deviations (RSD) of 0.7%, 2.8%, and 1.8%, respectively (Fig. S7B and Fig. S7E). To evaluate the long-term stability, the aptasensor was kept at 4 °C in the dark, where CM and EC responses were measured daily. After 7 days, the ΔC and I_{MB} with light off and on remained about 97.5%, 97.3%, and 96.7% of the initial signal values with lower RSD, respectively (Fig. S7C and Fig. S7F). These results display that the dual-modal aptasensor possesses considerable excellent reproducibility and stability.

Real sample analysis

To investigate the applicability and reliability of the developed dual-modal aptasensor, the detection of AFB1 was performed in spiked (0.005, 1, and 20 ng mL^{-1}) and moldy samples of peanut and soil (Fig. S8). As displayed in Table S2, the recoveries are in the range of 92.01–101.12% and 94.82–110.29% for CM and EC sensing modes, respectively, with an RSD below 5%. The results obtained by the developed dual-modal aptasensor are consistent with HPLC-FL, revealing the aptasensor possesses good reliability. These results verify the potential practical applications of the developed dual-modal aptasensor for AFB1 detection.

Captions

Fig. S1. (A) SEM images of rGO. (B) UV-vis spectrum of rGO. (C) Photocurrent response of rGO with variable light wavelengths (365–440 nm). (D) Photocurrent response of rGO with adjustable light intensity (0.7–7 W cm^{-2}) of 365 nm light source. (E) SEM images of rGO-AuNPs. (F) Stability of rGO-AuNPs.

Fig. S2. (A) Tauc plots of rGO and rGO-AuNPs. (B) VB-XPS spectra of rGO. (C) XPS full scan spectrum of rGO.

Fig. S3. (A) UV-vis spectra of Apt-Primer-MB (a) before and (b) after combining with SMBs. (B) Zeta potential of (a) Apt-Primer-MB, (b) SMBs, and (c) SMBs combined with Apt-Primer-MB. (C) Particle size distribution of (a) SMBs and (b) SMBs combined with Apt-Primer-MB.

Fig. S4. Characterization of the aptasensor fabrication process using (A) CVs in 0.1 M KCl solution containing 5 mM $[Fe(CN)_6]^{3-/4-}$, (B) CVs in 0.1 M PBS (pH 7.4) containing 0.1 M AA and 0.1 M KCl, (C) Bode plots, and (D) Bode phase angle plots: (a) bare GCE, (b) rGO-AuNPs/GCE, (c) Primer-Padlock-MB/rGO-AuNPs/GCE, and (d) MB/Primer-Padlock-MB/rGO-AuNPs/GCE.

Fig. S5. (A) Photographs of a portable colorimeter for CM sensing detection. (B) CM measurements in the presence of 0, 10, and 100 μg mL^{-1} AFB1. (C) ACV measurements toward 0.01 and 10 ng mL^{-1} AFB1 with light on and off. (D) Bode plots of GCE and rGO-AuNPs/GCE with light on and off.

Fig. S6. Optimization of experimental parameters by colorimetric measurement. (A) Combination time of SMBs and Apt-Primer-MB. (B) Incubation time of AFB1 and Apt-Primer-MB SMBs.

Fig. S7. CM mode of the proposed aptasensor: (A) selectivity tests by measuring 20 ng mL^{-1} AFB1 and 200 ng mL^{-1} solution of interferents including OTA, ZEN, FB1, and their mixture, (B) reproducibility tests by 7 parallel samples measurements of 20 ng mL^{-1}

AFB1, and (C) stability tests for 7 days by measuring 20 ng mL^{-1} AFB1. PEEC mode of the proposed aptasensor: (D) selectivity tests for 1 ng mL^{-1} AFB1 and 10 ng mL^{-1} solution of interferents, (E) reproducibility tests by 7 parallel measurements of 1 ng mL^{-1} AFB1, and (F) stability tests for 7 days by measuring 1 ng mL^{-1} AFB1.

Fig. S8. Photographs of real samples including fresh and moldy peanut and soil.

Table S1. Comparisons of the developed aptasensor with the reported sensor for AFB1 detection.

Table S2. Detection results of the developed aptasensor and validation by HPLC-FL for AFB1 in peanut and soil samples (n = 3).

Fig. S1

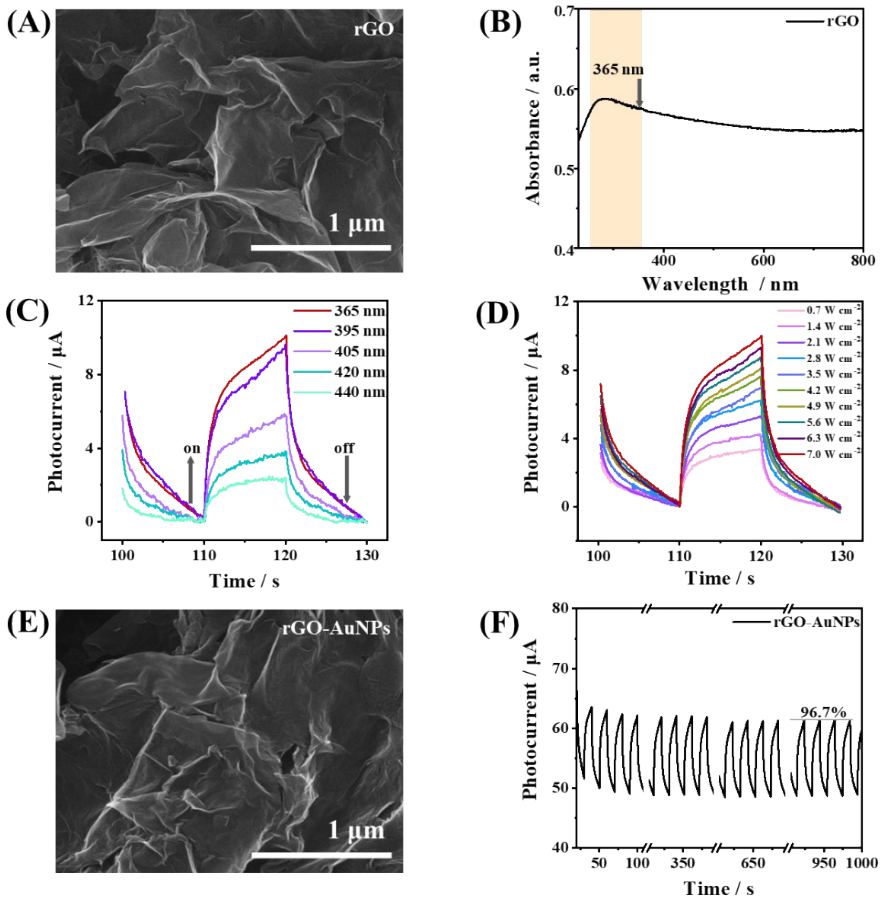
(A)
rGO
1 μm
(B)
rGO
365 nm
Absorbance / a.u.
Wavelength / nm
(C)
365 nm
395 nm
405 nm
420 nm
440 nm
on
off
Photocurrent / μA
Time / s
(D)
Photocurrent / μA
Time / s
(E)
rGO-AuNPs
1 μm
(F)
rGO-AuNPs
96.7%
Photocurrent / μA
Time / s

Fig. S2

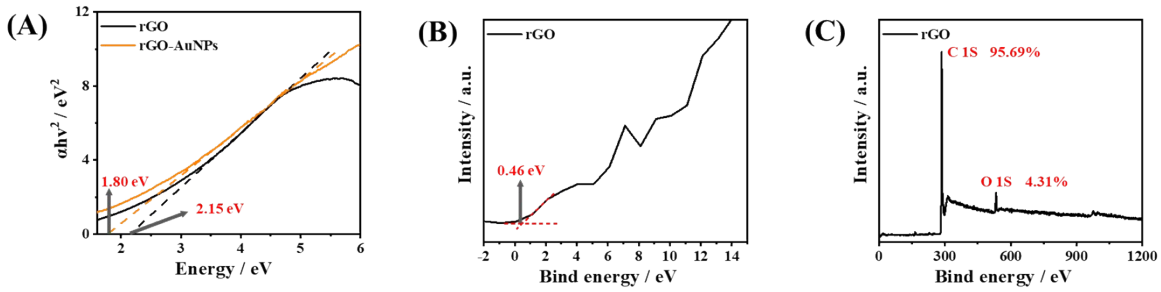
(A)
rGO
rGO-AuNPs
1.80 eV
2.15 eV
αhν² / eV²
Energy / eV
(B)
rGO
0.46 eV
Intensity / a.u.
Bind energy / eV
(C)
rGO
C 1S 95.69%
O 1S 4.31%
Intensity / a.u.
Bind energy / eV

Fig. S3

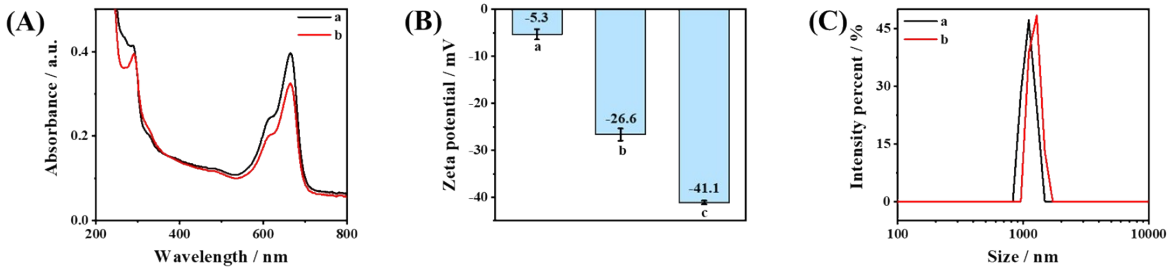
(A)
Absorbance / a.u.
Wavelength / nm
a
b
(B)
Zeta potential / mV
-5.3
-26.6
-41.1
a
b
c
(C)
Intensity percent / %
Size / nm
a
b

Fig. S4

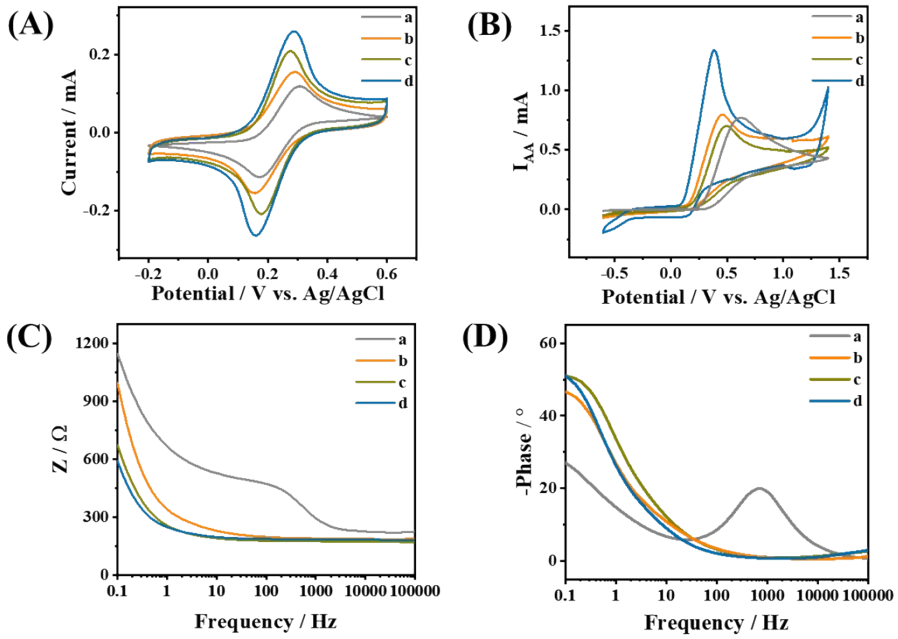
(A)
Current / mA
Potential / V vs. Ag/AgCl
(B)
$I_{\Delta A}$ / mA
Potential / V vs. Ag/AgCl
(C)
Z / Ω
Frequency / Hz
(D)
-Phase / °
Frequency / Hz
a
b
c
d

Fig. S5

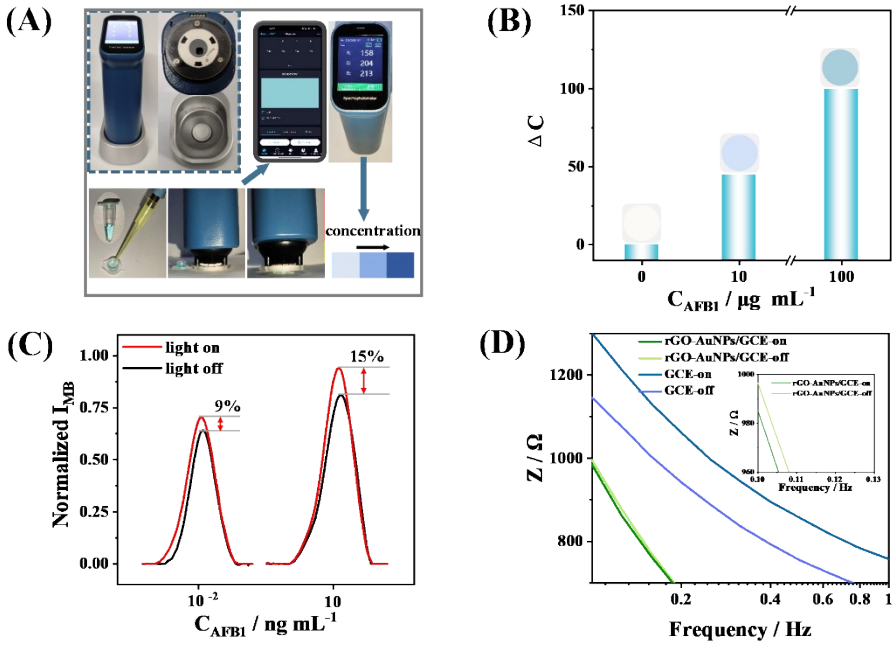
(A)
concentration
(B)
ΔC
150
100
50
0
0
10
100
C_AFB1 / μg mL^-1
(C)
light on
light off
9%
15%
Normalized I_MB
1.00
0.75
0.50
0.25
0.00
10^-2
10
C_AFB1 / ng mL^-1
(D)
rGO-AuNPs/GCE-on
rGO-AuNPs/GCE-off
GCE-on
GCE-off
Z / Ω
1200
1000
800
0.2
0.4
0.6
0.8
1
Frequency / Hz

Fig. S6

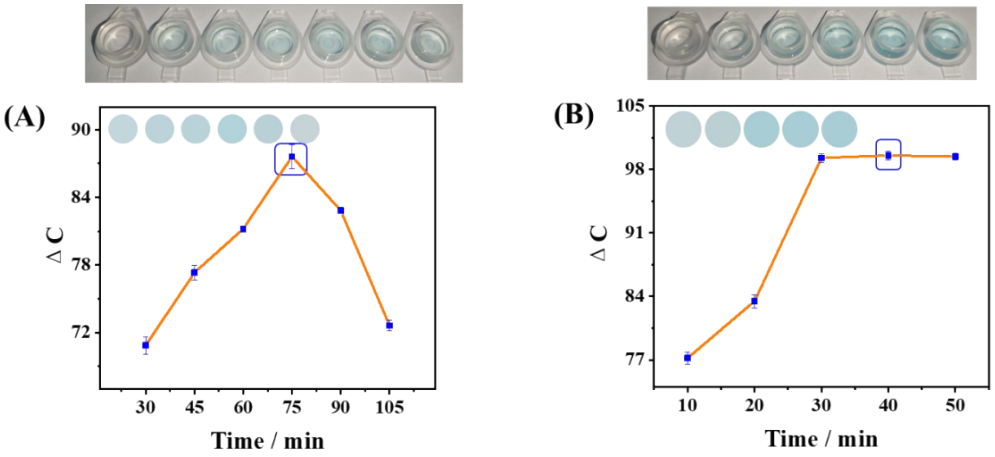
(A)
90
84
78
72
ΔC
30
45
60
75
90
105
Time / min
(B)
105
98
91
84
77
ΔC
10
20
30
40
50
Time / min

Fig. S7

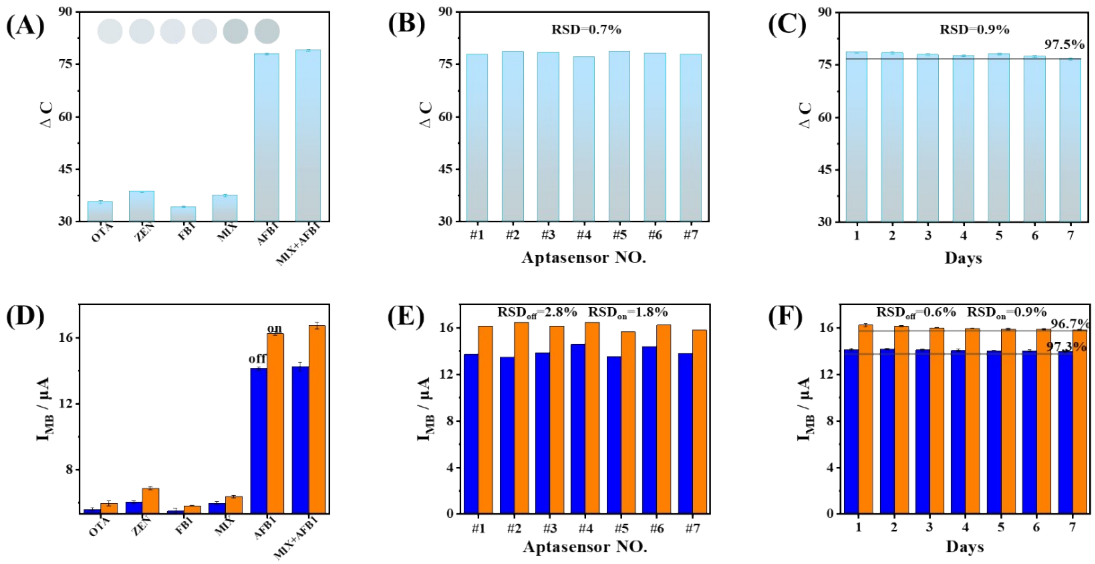
(A)
ΔC
OTA
ZEN
FBT
MIX
AFBT
MIX+AFBT
(B)
RSD=0.7%
Aptasensor NO.
(C)
RSD=0.9%
97.5%
Days
(D)
I_{MB} / μA
off
on
(E)
RSD_{off}=2.8% RSD_{on}=1.8%
Aptasensor NO.
(F)
RSD_{off}=0.6% RSD_{on}=0.9%
96.7%
97.3%
Days

Fig. S8

Table S1

Methods	Linear range (ng mL^{-1})	LOD (pg mL^{-1})	References
EC	$0.01–1.0 \times 10^2$	1.82	[12]
EC	0.05–20	16	[13]
EC	$0.01–1.0 \times 10^3$	0.73	[14]
CM	1–10	3.6×10^2	[15]
CM	$5–2.5 \times 10^2$	1.5×10^3	[16]
EC-CM	$0.05–2.0 \times 10^2$	0.43	[17]
PEEC-CM	**$1.0 \times 10^{-3}–1.0 \times 10^5$**	**0.12**	**Our work**

EC: electrochemical

CM: colorimetric

PEEC: photo-enhanced electrochemical

Table S2

Sample	Spiked (ng mL^{-1})	Developed aptasensor									HPLC-FL	
		CM			EC (light-off)			EC (light-on)				
		Detected (ng mL^{-1})	Recovery (%)	RSD (%)	Detected (ng mL^{-1})	Recovery (%)	RSD (%)	Detected (ng mL^{-1})	Recovery (%)	RSD (%)	Detected (ng mL^{-1})	Recovery (%)
Peanut	0	ND	-	-	ND	-	-	ND	-	-	ND	-
	0.005	-	-	-	-	-	-	0.0051	101.58	4.01	-	-
	1.0	-	-	-	1.09	109.12	2.68	1.10	110.29	3.03	1.06	106.00
	20	18.40	92.01	2.57	19.95	99.77	1.65	-	-	-	18.6	93.00
Moldy peanut	0	8.84		2.51	9.17		2.31	-	-	-	9.28	
Soil	0	ND	-	-	ND	-	-	ND	-	-	ND	-
	0.005	-	-	-	-	-	-	0.0051	102.10	3.63	-	-
	1.0	-	-	-	0.95	94.82	3.02	1.07	107.07	3.97	1.08	108.00
	20	20.22	101.12	4.21	20.87	104.36	2.71	-	-	-	18.1	90.50
Moldy soil	0	10.62		3.54	10.31		1.90	-	-	-	9.81	

“ND”: Not detected; “-”: Not in linear range; Moldy soil samples were taken from soil around moldy peanuts.

References

1. X. Wu, Y. Chai, R. Yuan, X. Zhong and J. Zhang, *Electrochim. Acta*, 2014, **129**, 441–449.
2. L. Wang, G. Liu, Y. Ren, Y. Feng, X. Zhao, Y. Zhu, M. Chen, F. Zhu, Q. Liu and X. Chen, *Anal. Chem.*, 2020, **92**, 14259–14266.
3. R. F. Albers, R. A. Bini, J. B. Souza, D. T. Machado and L. C. Varanda, *Carbon*, 2019, **143**, 73–84.
4. Z. Wu, X. Sun, X. Guo, Y. Ding, Y. Ou, H. Yang, Y. Chen, Y. Hu, D. Kuang, C. Zhao and Y. He, *ACS Appl. Mater. Interfaces*, 2021, **13**, 27188–27199.
5. X. Chen, H. Guo, T. Wang, M. Lu and T. Wang, *Electrochim. Acta*, 2016, **196**, 558–564.
6. F. Xiao, W. Li, L. Fang and D. Wang, *J. Hazard. Mater.*, 2016, **308**, 11-20.
7. S. Meng, D. Liu, Y. Li, N. Dong, S. Liu, C. Liu, X. Li and T. You, *J. Hazard. Mater.*, 2023, **441**, 129759.
8. Y. Zhang, J. Du, Z. Wang, M. Luo, Y. Tian, T. Fujita, Q. Xue and M. Chen, *ACS Appl. Energy Mater.*, 2018, **1**, 2183–2191.
9. D. Zhu and Q. Zhou, *Appl. Catal. B*, 2020, **268**, 118426.
10. Y. Zhou, S. Lv, X. Y. Wang, L. Kong and S. Bi, *Anal. Chem.*, 2022, **94**, 14492–14501.
11. S. G. Chavan, A. K. Yagati, M. Mohammadniaei, J. Min and M. H. Lee, *Anal. Chem.*, 2019, **91**, 5841–5849.
12. T. Zhong, S. Li, X. Li, Y. JiYe, Y. Mo, L. Chen, Z. Zhang, H. Wu, M. Li and Q. Luo, *Food Chem.*, 2022, **384**, 132495.
13. Y. Li, D. Liu, C. Zhu, X. Shen, Y. Liu and T. You, *J. Hazard. Mater.*, 2020, **387**, 122001.
14. Y. Jin, Y. Luan, Z. Wu, W. Wen, X. Zhang and S. Wang, *Anal. Chem.*, 2021, **93**, 13204–13211.
15. J. Lerdsri, W. Chananchana, J. Upan, T. Sridara and J. Jakmunee, *Sens. Actuators B Chem.*, 2020, **320**, 128356.
16. W. Zhu, L. Li, Z. Zhou, X. Yang, N. Hao, Y. Guo and K. Wang, *Food Chem.*, 2020, **319**,

126544.

17. J. Qian, C. Ren, C. Wang, K. An, H. Cui, N. Hao and K. Wang, *Biosens. Bioelectron.*, 2020, **166**, 112443.